Dynamical Plasma Response during Driven Magnetic Reconnection

J Egedal,* A Fasoli,† and J Nazemi

Massachusetts Institute of Technology, Plasma Science and Fusion Center, Cambridge, Massachusetts 02139

(Received 9 April 2002; revised manuscript received 25 November 2002; published 3 April 2003)

Direct measurements of a collisionless current channel during driven magnetic reconnection are obtained for the first time on the Versatile Toroidal Facility. The size of the diffusion region is found to scale with the electron drift orbit width, independent of the ion mass and plasma density. Based on experimental observations, analytic expressions governing the dynamical evolution of the current profile and the formation of the electrostatic potential that develops in response to the externally imposed reconnection drive are established. This time response is closely linked to the presence of ion polarization currents.

DOI: 10.1103/PhysRevLett.90.135003 PACS numbers: 52.35.Vd, 52.72.+v

Fast changes of magnetic field topology are observed in association with reconnection phenomena [1] both in space and laboratory plasmas, e.g., in solar flares [2], magnetic substorms at the geomagnetic tail [3], and in the case of internal disruptions in fusion tokamak devices [4]. Among the main outstanding open issues in the physics of reconnection are the origin of the observed fast time scales, characteristic in weakly collisional plasmas, and the mechanisms by which magnetic energy is transformed into plasma kinetic energy. Both issues are intimately related to the dynamics of the plasma response in the proximity of the reconnection region.

In this Letter, we show the first direct experimental observations of the plasma dynamical response to driven reconnection in a collisionless plasma. Despite a constant, externally imposed reconnection drive, we show that the reconnection does not proceed in a steady-state manner, but the current channel sustained by the plasma is subject to strong variations both in intensity and geometry.

The experiments are performed on the collisionless plasmas produced in the Versatile Toroidal Facility (VTF) [5]. Compared to other dedicated reconnection experiments [6–13], a number of features render the VTF experiment unique: The plasma is created independently of the reconnection process via electron cyclotron resonance heating by applying up to 50 kW of rf power at a frequency of 2.45 GHZ. This scheme permits the production of highly reproducible discharges with temperature of the order of $T_e \simeq 20$ eV and densities up to $n \simeq 4 \times 10^{17}$ m^{-3}. Hence, the VTF plasmas are characterized by a collisionless regime where the mean free path of the electrons, $\lambda_e \simeq 50$ m, is much larger than the dimensions of the device. Furthermore, the toroidal geometry eliminates undesirable electrostatic sheath effects characteristic of linear experiments [8]. In order to reconstruct the full time evolution of the plasma response, reconnection is driven in VTF during a time much longer than the characteristic time predicted by the Sweet-Parker model [14,15].

The magnetic configuration of the VTF experiment is a toroidal cusp where the poloidal magnetic field, $\mathbf{B}_{\text{cusp}}$, is described by an X-configuration with an absolute magnetic null for $(R, Z) = (0.98, 0)$ m. The strength of the poloidal field is characterized by $|\nabla B_{\text{cusp}}|$. In addition to the poloidal magnetic field, a toroidal guide magnetic field, B_g, may be applied. The ratio between the cusp field and the guide field is given by r/l_0, where $l_0 = B_g/|\nabla B_{\text{cusp}}|$ and r is the distance from the X-line.

The reconnection drive is produced by the transformer action of a solenoid installed at the center of the device. The maximum driven reconnection rate is $E_\phi \simeq 10$ V/m, which is maintained in nearly steady-state up to 1 ms.

The profiles of the number density, current density, and electrostatic potential are obtained by movable electrostatic and magnetic probe arrays [16]. Data are collected during a large number of discharges, taking advantage of the high degree of shot-to-shot reproducibility. The data in Fig. 1 represents the measured time evolution of these profiles for a hydrogen plasma for $B_g \simeq 0.087$ T and $l_0 = 7$ m. The data corresponds to the initial phase after the reconnection drive is switched on at $t = 0$. The profiles of the three components of $\mathbf{B}$ are obtained from magnetic probe measurements. The plasma currents are calculated through $\mu_0 \mathbf{j} = \nabla \times \mathbf{B}$, assuming toroidal symmetry. The dashed lines in all the subfigures represent magnetic field lines, inferred on the basis of the toroidal plasma current profile and the currents applied in the VTF coil sets [16]. Two magnetic field lines, corresponding to one particular value of the poloidal magnetic flux function Ψ, are highlighted in pink so that they can be followed in time as they drift together, reconnect, and drift apart.

The first column of profiles represents the evolution of the plasma density. Because of the nature of the plasma production, a region of increased density is observed for $R > 1$ m, $Z < 0$ m, and $t = 0$ μs. As time progresses, this area of increased density can be followed as it propagates along with the magnetic field lines, which move in the poloidal cross section and undergo reconnection. The

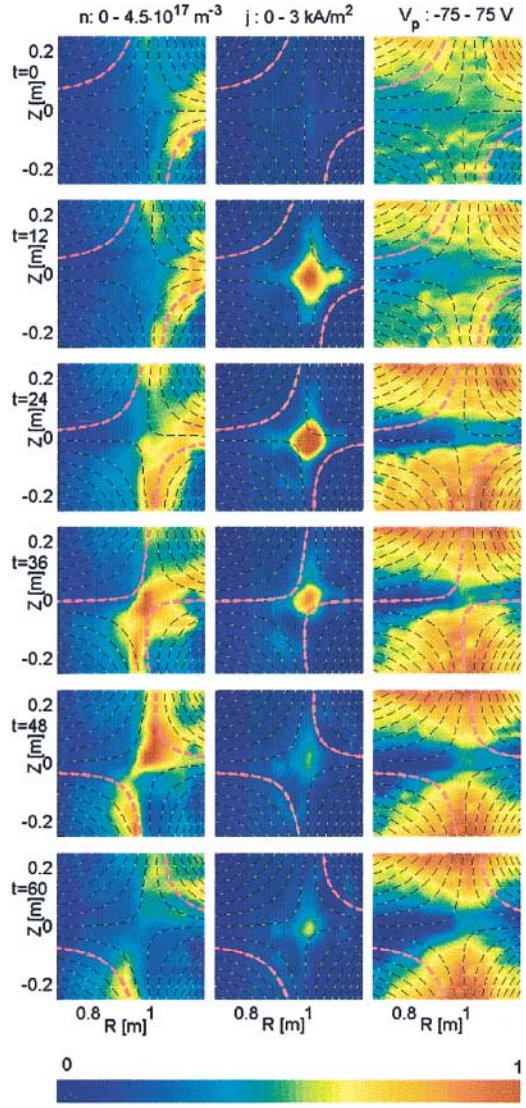

FIG. 1 (color). Measured contours of density, plasma current, and electrostatic potential during the initial phase of the forced reconnection pulse. Each row of subfigures corresponds to a snapshot in time as indicated in the left hand side. Between each row, the time is incremented by 12 μs.

inflow and outflow velocity is given by the $E \times B$ velocity imposed by the external reconnection drive.

The second column shows the temporal evolution of the current profile. For $t = 12$ μs and $t = 24$ μs, the data reveals a characteristic diamond shaped profile. The current density does not exceed $3\mathrm{kA/m^2}$. This value is about 3 orders of magnitude lower than the value E/η_s, where η_s is the Spitzer resistivity, calculated using the measured electron temperature.

The third column in Fig. 1 shows the evolution of the electrostatic potential, Φ. The potential evolves towards a configuration where $\mathbf{E} \cdot \mathbf{B} = 0$ away from the X-line [17].

With the knowledge of the electrostatic potential, Φ, it is possible to infer the total electric field $\mathbf{E} = -\nabla\Phi - \partial\mathbf{A}/\partial t$, hence the size of the diffusion region where $\mathbf{E} \cdot \mathbf{B} \neq 0$ (here $\mathbf{A}$ is the magnetic vector potential). In Figs. 2(a)–2(c) the measured contours of $\mathbf{E} \cdot \mathbf{B}$ are shown for Neon, Krypton, and Xenon plasmas. The size of the diffusion region is independent of the ion mass. This conclusion is also supported by other measurements in Hydrogen, Helium, Nitrogen, and Argon plasmas (not shown).

The number density of the plasma can be varied by changing the rf heating power. The size of the diffusion regions is also found to be independent of the number density (comparing the two last rows of Fig. 1). Hence, the size of the diffusion region does not scale with the electron or the ion inertial skin depths, $c/\omega_{e,i}$, and it is independent of the Larmor radii, ρ_i and $\rho_s = \sqrt{m_i T_e}/(qB)$. Furthermore, the shape of the current channel is different from the typical elongated Harris sheet observed in other experiments in the more collisional regimes [18], and its size largely exceeds the Larmor radius of the electrons ρ_e.

In [17] the high rates of reconnection observed in VTF were found consistent with a large neoclassical resistivity, caused by the absence of passing particles. Furthermore, in [19] it was found that within a distance from the X line given by the electron drift orbit width, $\rho_{\mathrm{cusp},e} = \sqrt{\rho_e l_0}$, the electrons do not follow the magnetic field lines. The electrons are therefore not effective in "short circuiting" the electric fields along $\mathbf{B}$. In agreement with the predictions of Ref. [19], Fig. 2(d) contains data that suggest that the width of the diffusion region scales with $\rho_{\mathrm{cusp},e}$.

We introduce the following expression to fit the measured profiles of the electrostatic potential $\Phi \simeq E_\phi F(R, Z)$, where

$$F = \frac{1}{4} l_0 \log\left(\frac{[(R - R_0)^2 + \delta^2]^\alpha}{[Z^2 + \delta^2]^{2-\alpha}}\right). \quad (1)$$

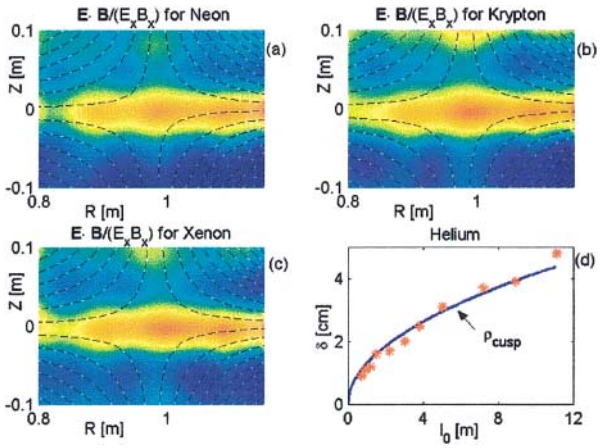

FIG. 2 (color). (a)–(c): Contours of $\mathbf{E} \cdot \mathbf{B}$ for three different filling gases, calculated on the basis of the measured total electric field $\mathbf{E} = -\partial\mathbf{A}/\partial t - \nabla\Phi$. The shape and size of the diffusion region is observed to be independent of the ion mass. (d) The width, δ, of the diffusion region is observed to scale with the drift orbit width of the electrons, $\rho_{\mathrm{cusp},e} = \sqrt{\rho_e l_0}$.

Such expression represents an extension of the form found to describe the potential in the ideal region, where $\mathbf{E} \cdot \mathbf{B} = 0$ (see Ref. [17]), and it coincides with it in that part of the cross section for which $|(R - R_0)Z| > \delta^2$. The inclusion of the parameter δ is needed to model the width of the diffusion region, while the parameter α accounts for its elongation [see Figs. 2(a)–2(c)]. Typical values for these parameters are $\delta = \rho_{\mathrm{cusp},e}$ and $\alpha = 0.7$.

To explore the temporal behavior of the current channel we apply an oscillatory reconnection drive, V_{drive}, with a frequency of 15 kHz. The plasma responds with an oscillating toroidal current channel. The loop voltage, V_{loop}, is the sum of the external drive and the toroidal electric field induced by the oscillating toroidal current. Figure 3(c) shows the time traces of the external reconnection drive, the loop voltage, and the toroidal current as measured by a Rogowsky coil encircling the X-point region.

The time behavior of the current profile is approximated through the expression

$$j(R, Z, t) = V_{\mathrm{loop}}(t)\, j_1 + dV_{\mathrm{loop}}(t)/dt\, j_2, \tag{2}$$

where the time independent profiles j_1 and j_2 (with units $\mathrm{AV}^{-1}\,\mathrm{m}^{-2}$ and $\mathrm{CV}^{-1}\,\mathrm{m}^{-2}$, respectively) are shown in Figs. 3(a) and 3(b). As indicated in the figure, the profile of j_1 [j_2] is obtained from the time average of the measured current profiles corresponding to a time interval where the average of dV_{loop}/dt [V_{loop}] vanishes.

The profile j_2 of electron currents is related to the ion polarization currents, $j_\perp$, given by

$$j_\perp = -\frac{nm}{B^2}\,\nabla_\perp\!\left(\frac{d\Phi}{dt}\right). \tag{3}$$

The role of the electron current along field lines is to close the path of the current such that quasineutrality is maintained [20]. Using $\nabla \cdot (j_\perp + j_\parallel) = 0$, we obtain the following expression for these field aligned currents

$$j_\parallel = \frac{dV_{\mathrm{loop}}}{dt}\,\frac{1}{2\pi R_0}\int_{\mathrm{wall}}^{(R,Z)} \frac{nm}{B^2}\,\nabla_\perp^2 F\, dl_\parallel, \tag{4}$$

where the integration is carried out along field lines. This solution has the appropriate form $j_\parallel = dV_{\mathrm{loop}}/dt\, j_{2,\mathrm{theory}}$. The theoretical profile $j_{2,\mathrm{theory}}$, which nearly coincides with the measured profile of j_2, is shown in Fig. 3(c).

Further insight into the time behavior of the loop voltage and the total toroidal current is obtained by integrating Eq. (2) over the poloidal cross section:

$$I_{\mathrm{tot}} = V_{\mathrm{loop}}/R_{j1} + C_{j2}\, dV_{\mathrm{loop}}/dt, \tag{5}$$

where $1/R_{j1} = \int j_1 dA$, $C_{j2} = \int j_2 dA$, and $dA = dRdZ$. In turn, the loop voltage may be written as $V_{\mathrm{loop}} = V_{\mathrm{drive}} - LdI/dt$, where V_{drive} is the contribution from the external coils and $L = \mu_0 R_0[\log(R_0/\delta) + 0.329] \simeq 5\mu H$ is the self-inductance of a current loop with major radius R_0 and minor radius δ. We thus find the following second order differential equation for the temporal evolution of the loop voltage

$$V_{\mathrm{loop}} = V_{\mathrm{drive}} - \frac{dV_{\mathrm{loop}}}{dt}\frac{L}{R_{j1}} - \frac{d^2 V_{\mathrm{loop}}}{dt^2} LC_{j2}. \tag{6}$$

Equations (5) and (6) successfully reproduce the time response of the total toroidal current both to a steady and an oscillating reconnection drive. An example is shown in Fig. 4(a) where the measured current response (to a steady drive) in an argon plasma is accurately reproduced through curve fitting with R_{j1} and C_{j2} as the only free parameters.

Furthermore, using Eq. (4) it can be shown that the $C_{j2} \propto (nm/B^2)(l_0/\delta)^2$. Applying $\delta = \rho_{\mathrm{cusp},e}$ we obtain $C_{j2} \propto nml_0/B^2$. As summarized in Figs. 4(b) and 4(c) this scaling for C_{j2} has been verified through a systematic study of the current response in a variety of plasmas with different values of n, m, and l_0. The values of n (indicated in the figure) used in calculating the theoretical lines of

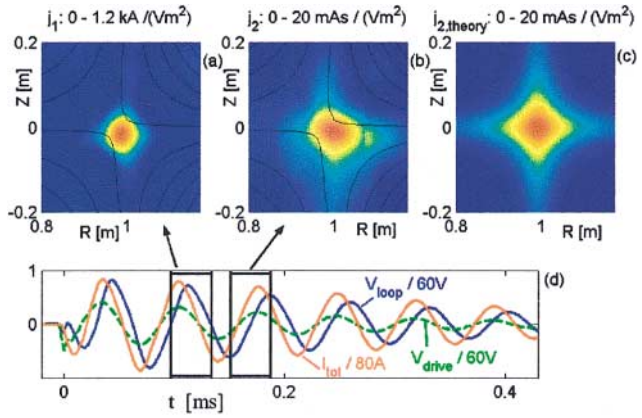

FIG. 3 (color). The current profile is approximated by the form $j(R, Z, t) = V_{\mathrm{loop}}(t)\, j_1 + dV_{\mathrm{loop}}(t)/dt\, j_2$. Experimental profiles of j_1 and j_2 are given in (a) and (b). The theoretical profiles of j_2 is shown in (c). In (d) the plasma response (total current and the loop voltage) to an external drive V_{derive} is shown.

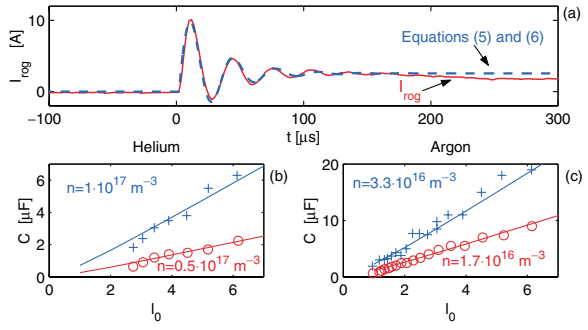

FIG. 4 (color). (a): The red curve is total toroidal current in response to a steady reconnection drive. The blue is the fitted response using Eqs. (5) and (6). (b),(c): Fitted values of C_{j2} confirming the theoretical scaling $C_{j2} \propto nml_0$.

C_{j2} are consistent with our Langmuir probe density measurements.

In analogy with simple LCR circuits, R_{j1} provides the damping of the oscillations. Empirically we find that $R_{j1} \propto 1/(nl_0)$. For the hydrogen plasma considered in Fig. 1 we have $L/R_{j1} > 4R_{j1}C_{j2}$, consistent with the current profile settling without oscillations. In argon plasmas (where C_{j2} is increased due to the higher mass) we find $L/R_{j1} < 4R_{j1}C_{j2}$, in agreement with the oscillatory response in Fig. 4(a).

In order to determine which physical mechanism is responsible for breaking the frozen-in condition, we consider the momentum balance in the diffusion region in terms of the generalized Ohm's law,

$$\mathbf{E} + \mathbf{v} \times \mathbf{B} = \eta \mathbf{j} + \frac{1}{ne}(\mathbf{j} \times \mathbf{B} - \nabla \cdot \mathbf{p}_e) + \frac{m_e}{ne^2}\frac{d\mathbf{j}}{dt}. \quad (7)$$

Of particular interest is the component parallel to the X line. For the observed low current densities $\eta j_\phi \simeq 0.01$ V/m. The resistive term is therefore completely inadequate to explain the rate of reconnection, $E_\phi \simeq 10$ V/m.

An experimental Ohm's law where the momentum balance of the electrons is obtained through turbulence induced anomalous resistivity requires η_{anoma} to cover all values from $-\infty$ to ∞ and to be described by a complicated function of (dV_{loop}/dt, V_{loop}, n, m, l_0). In contrast, we find that the size or the shape of the diffusion region only depend on l_0. Hence, the structure of the diffusion region is independent of the force free current, the level of which varies with dV_{loop}/dt. Our data do therefore not support turbulence induced anomalous resistivity, but are consistent with a generalized Ohm's law, which apart from the negligible ηj- term, do not depend on the force free currents.

Within the diffusion region the guide magnetic field is more than 100 times larger than the cusp magnetic field. Consequently, the Hall term, $\mathbf{j} \times \mathbf{B}/(ne)$, does not contribute to the momentum balance in the direction of the X line.

The observed current profiles and the modifications in the density along field lines due to the ion polarization currents are similar to those observed in Refs. [20,21]. However, the pressure gradients associated with these density variations do not account for the observed high rates of reconnection. It is here noteworthy that the open boundary conditions in VTF differs significantly from the periodic boundaries often used in numerical simulations. The open boundaries allow the potential Φ to develop. It is this potential that ensures that $\mathbf{E} \cdot \mathbf{B} = 0$ throughout the most of the of the poloidal cross section.

Our finding that the width of the diffusion region scales with $\rho_{\text{cusp},e}$ is a strong indication that the kinetic effects related to the drift orbits of the electrons are responsible for breaking the frozenin law. Further investigations are planned to measure and calculate the distribution function of the electrons in order to explore how orbit kinetic effects possibly translate into finite $\nabla \cdot \mathbf{p}_e$- and $d\mathbf{j}/dt$ terms.

In summary, the detailed evolution of the profiles of plasma density, current density, and electrostatic potential at the onset of driven reconnection has been reconstructed experimentally in the collisionless regime, for the first time. An analytic description of the temporal evolution of the current profile, the electrostatic potential, and the associated ion polarization currents is derived and verified experimentally. The size of the diffusion region is inferred from the detailed knowledge of the electrostatic potential, and is shown to scale with the drift orbit width of the electrons, insensitive to the ion mass and plasma density.

The authors would like to thank Professor M. Porkolab and Dr. K. Hallatschek, Dr. P. Catto, and Dr. J. Ramos for inspiring discussions and support. This work is partly funded by the DoE Award No. DE-FG02-00ER54601.

*Email address: jegedal@psfc.mit.edu
†Also at CRPP-EPFL, CH-1015, Lausanne, Switzerland.

[1] J.W. Dungey, Philos. Mag. **44**, 725 (1953).
[2] S. Masuda, T. Kosugi, H. Hara, and Y. Ogawara, Nature (London) **371**, 495 (1994).
[3] V.M. Vasyliunas, Rev. Geophys. Space Phys. **13**, 303 (1975).
[4] J. B. Taylor, Rev. Mod. Phys. **28**, 243 (1986).
[5] J. Egedal, A. Fasoli, M. Porkolab, and D. Tarkowski, Rev. Sci. Instrum. **71**, 3351 (2000).
[6] D. Overskei and P. A. Politzer, Phys. Fluids (1958–1988) **19**, 683 (1976).
[7] G.G. Zukakishvili, I.F. Kavartskhava, and L.M. Zukakishvili, Sov. J. Plasma Phys. **4**, 405 (1978).
[8] R. L. Stenzel and W. Gekelman, J. Geophys. Res. **86**, 649 (1981).
[9] A.T. Altyntsev, V.M. Bardakow, V.I. Krasov, N.V. Lebedev, and V.L. Paperni, Sol. Phys. **106**, 131 (1986).
[10] S.V. Bulanov and A.G. Frank, Sov. J. Plasma Phys. **18**, 797 (1992).
[11] Y. Ono, M. Yamada, T. Akao, T. Tajima, and R. Matsumoto, Phys. Rev. Lett. **76**, 3328 (1996).
[12] M. Yamada, H.T. Ji, S. Hsu, T. Carter, R. Kulsrud, N. Bretz, F. Jobes, Y. Ono, and F. Perkins, Phys. Plasmas **4**, 1937 (1997).
[13] M. R. Brown, Phys. Plasmas **6**, 1717 (1999).
[14] P. A. Sweet, Nuovo Cimento Suppl. **8**, Ser. X, 188 (1958).
[15] E. N. Parker, J. Geophys. Res. **62**, 509 (1957).
[16] J. Egedal, A. Fasoli, D. Tarkowski, and A. Scarabosio, Phys. Plasmas **8**, 1935 (2001).
[17] J. Egedal and A. Fasoli, Phys. Rev. Lett. **86**, 5047 (2001).
[18] H. Ji, M. Yamada, S. Hsu, and R. Kulsrud, Phys. Rev. Lett. **80**, 3256 (1998).
[19] J. Egedal, Phys. Plasmas **9**, 1095 (2002).
[20] R. Kleva, J. Drake, and F. Waelbroeck, Phys. Plasmas **2**, 23 (1995).
[21] A. Aydemir, Phys. Fluids B **4**, 3469 (1992).